

Integrated and Steerable Vortex Lasers

B. Bahari, F. Vallini, T. Lepetit, R. Tellez-Limon, J. H. Park, A. Kodigala, Y. Fainman, and B. Kanté

Department of Electrical and Computer Engineering, University of California San Diego, La Jolla, CA 92093-0407, USA

bkante@ucsd.edu

Abstract- Orbital angular momentum is a fundamental degree of freedom of light that manifests itself even at the single photon level. The coherent generation and steering of structured light usually requires bulky and slow components. Using wave singularities known as bound states in continuum, we report an integrated device that simultaneously generates and steers powerful coherent beams carrying orbital angular momentum. The device brings unprecedented opportunities in the manipulation of micro-particles and micro-organisms not only by allowing their remote trapping and rotation but also by enabling their translation. The proposed system will also find applications in areas such as biological sensing, microscopy, astronomy, and high-capacity communications.

Vortices are recognized to be ubiquitous features around wave singularities, forming threads of silence in acoustic, turbulences in superfluids, and tidal waves in oceans [1-2]. Light carrying Orbital Angular Momentum (OAM) has been intensively investigated due to interest in numerous fields including metrology, microscopy, quantum entanglement, and particle trapping [3-6]. The theoretically unlimited orthogonal basis of OAM spatial modes makes it a candidate to overcome the data transmission capacity crunch [7]. In 1992, Allen *et al.* demonstrated that beams with non-zero OAM have a “doughnut”-shaped intensity profile and carry a discrete OAM of $l\hbar$ per photon that results from the $e^{il\phi}$ dependence where ϕ is the azimuthal angle, \hbar the reduced Planck constant, and the integer l is called the topological charge [8].

On one hand, OAM in light is generally generated using non-integrated and unwieldy optical components that shape the phase front of a Gaussian laser beam. Generation methods include spiral phase plates [9], chiral dielectric meta-holograms [10], spatial light modulators [11], or metasurfaces [12-15]. Recently an interesting micro-ring laser operating at a parity-time-symmetry based Exceptional Point (EP) was demonstrated [16]. However, the strict requirement of EP operation severely limits the pump power to the single value ensuring the loss/gain balance, which in turn limits the output power of the laser. Additionally, any deviation from that single pump power value results in the generation of two OAM beams carrying opposite topological charges that cancel each other. Many applications, including particle trapping and light detection and ranging (LIDAR), have minimum power requirements and would benefit from a scalable and integrable vortex beam source.

On the other hand, beam steering, i.e., the ability to steer energy in controllable directions, has long been pursued and is usually implemented by optical phased arrays [17-19] using technologies such as liquid crystals [20], acousto-optics [21], and electro-optics [22-23]. Although Micro-Electro-Mechanical Systems (MEMS) have been recognized as a practical solution [24], state-of-the-art optical beam steering uses mechanisms that control the phase/intensity profile of individual nanoantennas for beam forming [17]. These mechanisms also suffer from limitations such as complexity, poor agility, and large size of non-integrated components. Furthermore, steering is usually limited to regular Gaussian beams.

The simultaneous generation and steering of coherent vortex beams from a single, scalable, and integrated source would constitute a major step forward, as it will enable the full and remote optical manipulation of micro-particles and micro-organisms not only by allowing their remote trapping and rotation but also by enabling their translation.

Here, we report an integrated photonic structure that is capable of simultaneously generating and steering coherent vortex beams in multiple and arbitrary directions controlled by the symmetry of the photonic structure. The vortex beam originates from a singularity where destructive interference occurs between radiative channels of the system [25-29].

The schematic of the device is shown in Fig. 1A. It is made of structured InGaAsP multiple quantum wells epitaxially grown on an InP substrate, and tailored to emit around the telecommunication wavelength. The structure is fabricated by electron beam lithography followed by dry etching to form holes and thus constitutes a Photonic Crystal (PhC). The PhC is subsequently bonded on a flat glass substrate coated with a thin layer of PolyMethyl

MethAcrylate (PMMA). During the bonding process, PMMA infiltrates holes of the PhC. Finally, the InP substrate is removed by wet etching using hydrochloric acid (see Supplementary Material). Figure 1B shows a top scanning electron micrograph view of a device, illustrating the uniformity of the holes in the structure.

To understand the physics of the device, modes of the PhC are calculated using finite element method and experimentally measured by pumping the device with a high-energy laser and collecting the photoluminescence at different angles around the wavelength of 1.6 μm (see Supplementary Material). Figure 1C presents the three modes within the gain bandwidth of InGaAsP, and, a very good agreement is observed between the theoretical and the experimental band diagrams.

Mode 1 is a singly degenerate mode while modes 2 and 3 are doubly degenerate modes. By changing the radius of holes uniformly over the whole structure, all three modes shift spectrally. The quality factor of mode 1 is theoretically infinite at the center of the Brillouin zone (Γ point) and independent of the radius of holes as mode 1 is symmetry protected (Γ -locked). This type of mode (usually referred to as band-edge mode) has been extensively investigated in uniform PhC lasers that necessarily emit normal to the surface. Modes 2 and 3 can only have infinite quality factors if all radiation channels destructively interfere to form singular states, at reciprocal space points, known as bound states in continuum [30]. These singular states are robust vortex centers carrying non-zero topological charges [31-32], and a continuous change of parameters of the systems continuously tunes the destructive interference condition away from the Γ point, resulting in beam steering of mode 2 along ΓM and mode 3 along ΓX (see Fig. 2A). Perturbing such modes, for example by varying the radius of holes of an array, is thus a method to steer laser beams without using additional components, such as phase arrays [12,17] or breaking the symmetry of the system to generate an artificial band-edge mode [33]. In our system, all holes have the same size in an array, and, the required phase shift to steer the beam is naturally provided by phase-offset between Floquet-Bloch harmonics of the periodic structure. It is worth noting that the broken σ_z symmetry and the finite size of the realized samples limit the quality factor of modes 2 and 3 to very large but not infinite values, forming quasi-bound states in continuum (see Supplementary Material) [29,31,34].

Several devices with a range of radius of holes were fabricated to observe beam steering. The measurements are performed using a micro-photoluminescence setup in which the reciprocal space is obtained by Fourier transforming the image plane (see Supplementary Material). The devices are optically pumped with a pulsed laser ($\lambda = 1064 \text{ nm}$, $T = 12 \text{ ns}$ pulse at a repetition rate $f = 275 \text{ kHz}$). The evolution of the output power as a function of the pump power (light-light curve) for a representative sample confirms the threshold behavior and a clear transition from spontaneous emission to lasing (Fig. 2B). Figure 2C-F present reciprocal space images of the emission of four samples with decreasing radii. The center of the image represents the center of the Brillouin zone i.e., $k_x = k_y = 0$ (Γ point). For $R = 250 \text{ nm}$, the PhC supports only the Γ -locked mode. Figure 2C confirms normal emission from this sample. As the radius is decreased below $R = 250 \text{ nm}$, the steering of four lasing beams along ΓX is observed. They correspond mode 3, which has a large quality factor along ΓX , and the four beams stem from the four-fold symmetry of the

crystal (invariance under 90° rotation). The number of beams can be controlled by the symmetry of the crystal as well as by boundary conditions (see Supplementary Material). The steering angle further increases by decreasing the radius as seen in Fig. 2D-F. The emission angles are extracted from the reciprocal space images and the numerical aperture of the collecting objective. Blue dots in Fig. 2A represent the experimental emission angles, and, as can be seen, lasing occurs in directions of predicted high quality factors. The operating mode is selected by its spatial overlap with the optical gain and switches from mode 1 to mode 3 for $R \sim 250$ nm (see Supplementary Material).

Singular states resulting from full destructive interference carry a quantized topological charge (order of singularity) that can be controlled by the topology of the structure and mathematically refer to modes with singular far-field phase whose order can be identified by the far-field polarization twisting around the singular point in reciprocal space [31-32] or real space [35]. Figures 3A-F represent the experimental (A-C) and theoretical (D-F) far-fields of devices emitting at different angles. For $R = 180$ nm and $R = 225$ nm, mode 3 (ΓX -steering), emits at an angle with a tilted doughnut-shaped pattern. For $R = 250$ nm, only mode 1 (Γ -locked), emits with a doughnut-shaped far-field.

To experimentally demonstrate the topology of these emissions, we perform self-interference of the lasing beams (see Supplementary Material). The interference patterns comprise two inverted fork-shaped patterns and thus demonstrate a topological charge of +1 and -1 for modes 3 and 1, respectively (Fig. 3G-I).

Singularities are always created in pairs (due to charge conservation) (30). This is evident in Fig. 2A where a high quality factor mode that steers along ΓM is predicted. However, this mode was not observed so far as it experiences less effective gain than the ΓX -steering mode (see Supplementary Material). Since the existence of this mode is guaranteed by topology, it should be possible to observe lasing and steering along ΓM if the pump power is increased.

Figures 4A-F present the evolution of the reciprocal space image as a function of the pump power for samples supporting all three singular modes. For $R = 190$ nm, Fig. 4A clearly shows lasing along ΓX . As the pump power is increased, four additional spots appear along ΓM (Fig. 4B-C). Similarly, for $R = 225$ nm, additional spots appear (at a smaller angle) as the pump power is increased (Fig. 4D-F). These results demonstrate steering along ΓM . The modes can be further identified by their wavelength scaling. In Fig. 4G, the continuous lines represent the theoretical prediction of the wavelength of each mode with large quality factor as a function of the radius of holes. Dots represent measured wavelengths of emissions from the lasers and a good agreement with theory is observed.

We have demonstrated a topological light source that generates and steers coherent vortex beams from a fully integrated laser. The device, made of an array of holes in InGaAsP multiple quantum wells, operates at singular points where destructive interference occurs between radiative channels of the photonic structure. These points continuously move along lines in reciprocal space as a function of the radius of holes. The integrated system emits light with orbital

angular momentum that can be steered in arbitrary directions controlled by the symmetry of the crystal without requiring mechanical components or breaking the in-plane symmetry of the system for beam forming. The proposed scalable and steerable vortex beam source opens unprecedented opportunities in micro-particles and micro-organisms manipulation as it enables not only their remote trapping and rotation from powerful emitted beams but also their translation. The device will find applications in multiple areas such as biological sensing, microscopy, astronomy, and high-capacity communications.

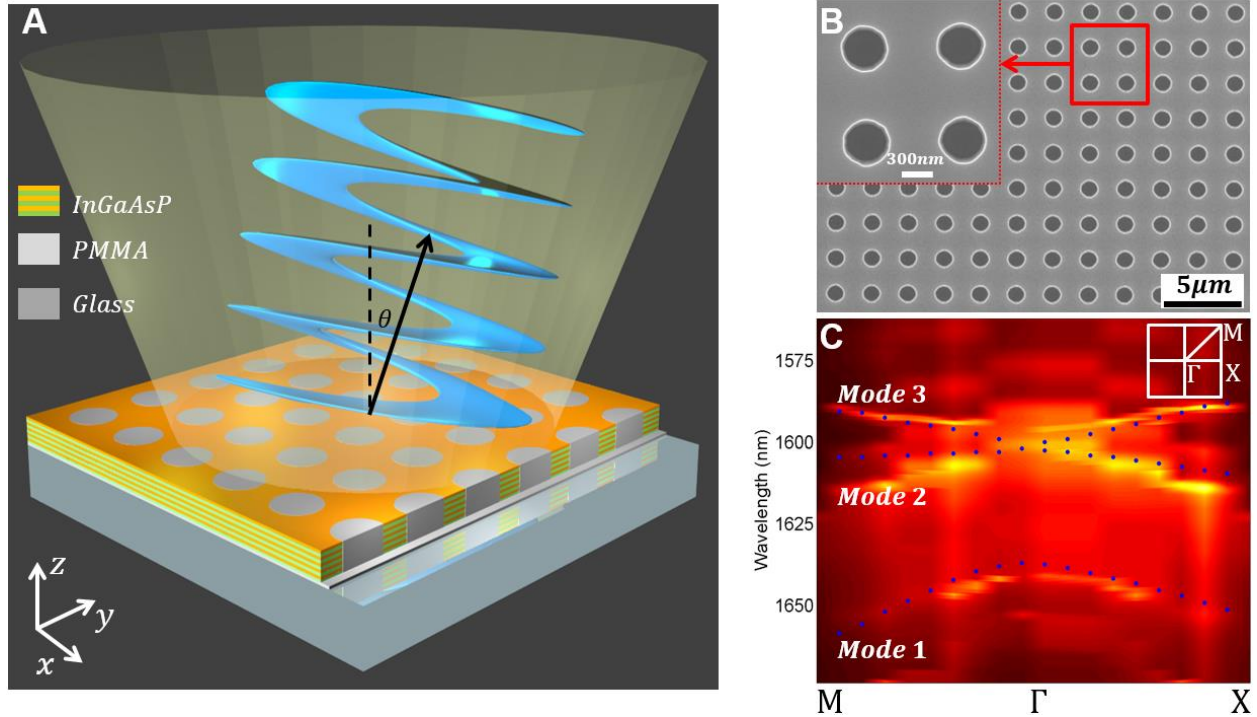


Figure 1 | Steerable coherent vortex beam source. (A) Schematic of the light source that is optically pumped (yellow beam) and generates a vortex beam at a controllable angle (blue beam). The structure is a square lattice photonic crystal (PhC) made of holes etched in InGaAsP multiple quantum wells bonded on a glass substrate coated with a thin layer of polymethyl methacrylate (PMMA). The holes are defined by electron beam lithography followed by wet etching. During the bonding process, PMMA infiltrates holes of the PhC. The InP substrate, on which InGaAsP is epitaxially grown, is subsequently removed by wet etching using hydrochloric acid (see Supplementary Information). (B) Top view scanning electron micrograph of a fabricated structure with a quantum well thickness of 300 nm, a period of 950 nm, and holes radius of 200 nm. (C) Experimental (color plot) and theoretical (blue dots) band diagrams measured/calculated along the Γ X and the Γ M directions. The experimental band diagram is measured by pumping the structure with a high-energy laser and collecting the photoluminescence at different angles (see Supplementary Information). A good agreement is observed between the theoretical band diagram (using finite element method) and experiments.

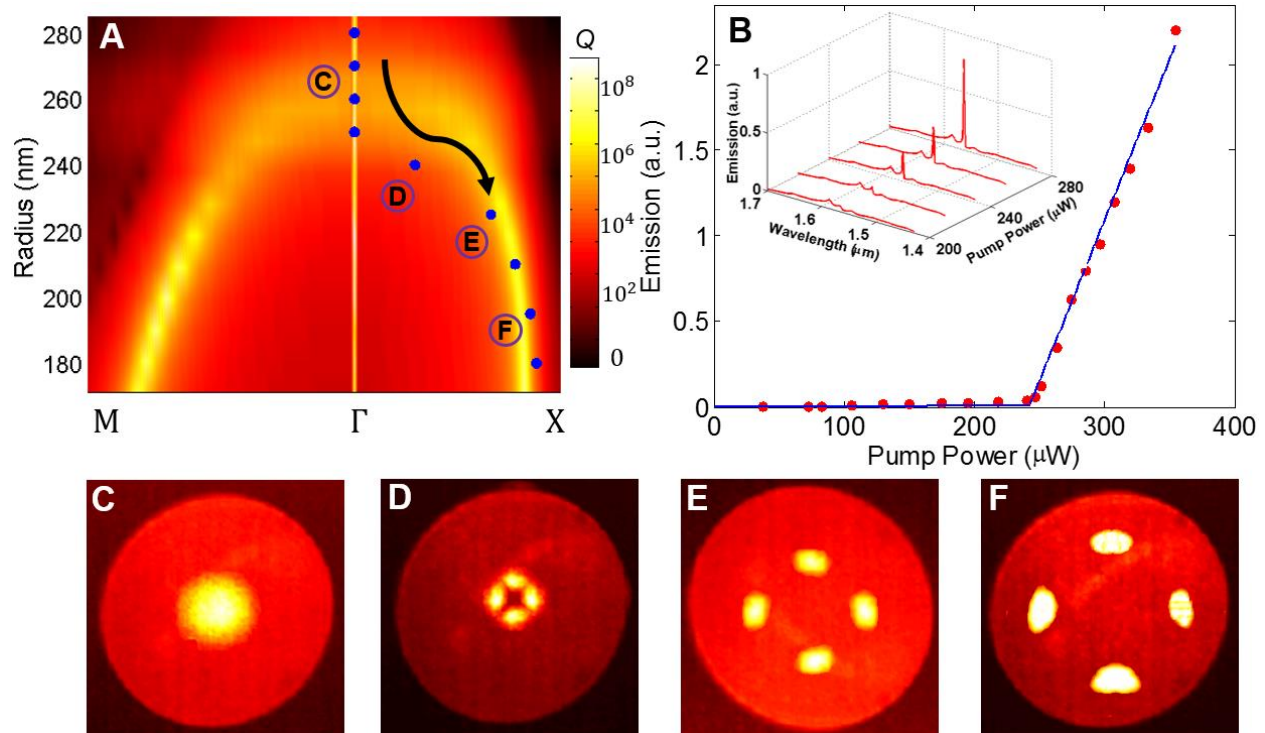


Figure 2 | Demonstration of beam steering in crystal's high-symmetry directions. (A) Quality factor (Q) of modes 1-3 as a function of the radius of holes in reciprocal space (k -space). The quality factors of modes 1, 2 and 3 are singular in k -space, at a point for mode 1 (Γ -locked), and along lines for mode 2 (steering along ΓM) and mode 3 (steering along ΓX). Modes 2 and 3 can thus continuously steer with the radius of holes. The quality factor of mode 1 is singular for all radii of holes because mode 1 is symmetry-protected while mode 2 and 3 become singular for holes radii smaller than $R \sim 250$ nm. Blue dots correspond to experimental measurements of the steering angle that have been extracted from k -space imaging (see Supplementary Information). The standard error in angle, from at least three measurements, is smaller than 0.5° . (B) Output power as a function of the average pump power (light-light curve) around the lasing wavelength for $R = 280$ nm. The red dots are experimental measurements of the output power for different pump powers. The blue solid lines are linear fits to the data in spontaneous and stimulated emission regimes and clearly show a threshold behavior, i.e. lasing. The inset shows the emission power evolution as a function of the pump power in a broader wavelength range. A similar light-light curve is measured for all other lasers (not shown). (C-F) Experimental k -space images of the emission from lasers with different radii. The distance of the bright spots to the center represents the in-plane wave-vector or equivalently the angle, and it increases as the radius of holes is decreased from $R = 250$ nm (c), to $R = 240$ nm (d), $R = 225$ nm (e), and $R = 190$ nm (f), clearly demonstrating steering of the lasing beam. The maximum angle in k -space imaging is given by the numerical aperture (NA) of the objective lens ($NA = 0.4$). The four-fold symmetry of the structure implies that any singularity is invariant under 90° rotation and this is confirmed by the four observed bright spots creating a 2-by-2 array of optical vortices (see Fig. 3).

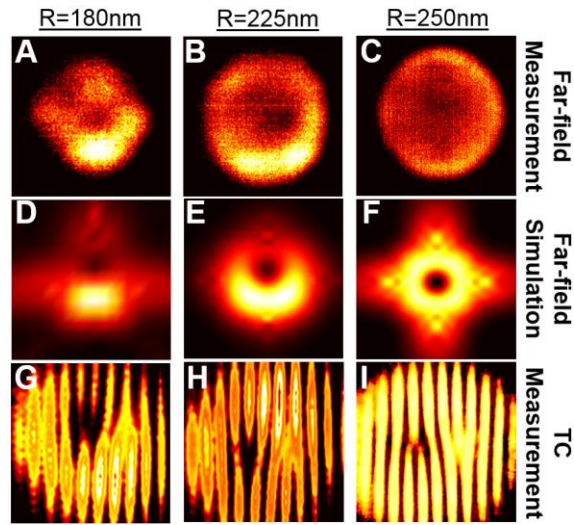


Figure 3 | Real space image of the vortex beams and topological charge measurement. Far-field radiation pattern measurements (A-C) and corresponding simulations (D-F) of the vortex lasers for three different radii, $R = 180$ nm (a, d), $R = 225$ nm (b, e), and $R = 250$ nm (c, f). By reducing the radius of holes, the far-field beam, which is doughnut-shaped, starts to steer. (G-I) Self-interference patterns of the emission beams for three samples with different radii. The two inverted fork-shape patterns demonstrate a topological charge (TC) of +1 for the mode steering along Γ_X (mode 3) and -1 for the Γ -locked mode (mode 1).

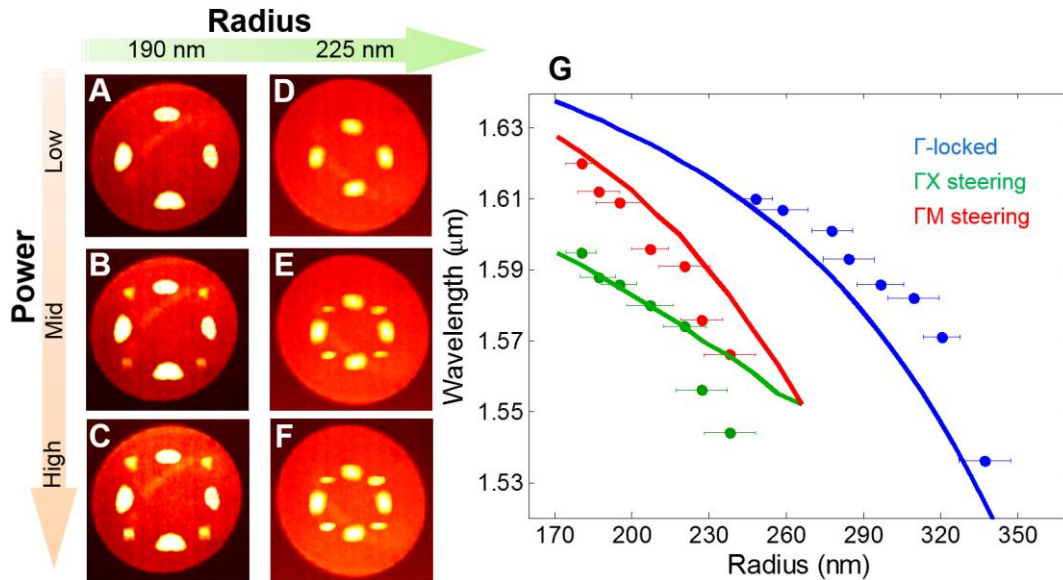


Figure 4 | Topological charge conservation and scaling of the lasers. (A-F) Reciprocal space images of the vortex laser when the only mode lasing is the one steering along Γ_X (mode 3) (A, D). This mode has a topological charge of +1, and, topology guarantees the existence of another mode with the opposite charge in the system, as charges are created in pairs. As the power is increased, it reaches the threshold of the mode steering along Γ_M (mode 2) that also starts to lase (B, E) as evident from the four additional bright spots (four-fold symmetry) in k-space appearing at 45° to the previous lasing spots. Increasing the pump power further, increases the emission power of the lasing modes, making them brighter (C, F). In our system, the threshold of the mode steering along Γ_M (mode 2, $\text{threshold}_{\Gamma_M}$) is larger than the threshold of the mode steering along Γ_X (mode 3, $\text{threshold}_{\Gamma_X}$) (see Supplementary Information). For pump powers smaller than $\text{threshold}_{\Gamma_X}$ ($\text{threshold}_{\Gamma_X} < \text{threshold}_{\Gamma_M}$), the mode steering along Γ_X is the only mode lasing in the device. The relative threshold of the modes is governed by their effective gain that depends not only on the modes distribution in the device but also the gain spectrum of the multiple quantum wells (see Supplementary Information). For $R = 190$ nm the emission angle of mode 2 is 13.5° and the emission angle of mode 3 is 11.1° . For $R = 225$ nm, the emission angle of modes 2 and 3 is 8° , demonstrating steering, both along Γ_X and Γ_M . (G) Lasing wavelength as a function of the radius of holes from 180 nm to 350 nm. Each point corresponds to a device with a specific radius. Error bars indicate the standard deviation of radii measured from fabricated devices. Solid lines represent the wavelength of the singularities (resonances with large quality factor) of mode 1 (blue), mode 2 (red), and mode 3 (green) for different radii of the holes. The good agreement between theory and experiment constitute an additional identification of the modes.

References:

1. Berry, M. Making waves in physics. *Nature* **403**, 21 (2000).
2. Nye, J. F. Natural focusing and the fine structure of light, *CRC Press* (1999).
3. Dorn, R., Quabis, S. & Leuchs, G. Sharper Focus for a Radially Polarized Light Beam. *Phys. Rev. Lett.* **91**, 233901 (2003).
4. Mair, A., Vaziri, A., Weihs, G. & Zeilinger, A. Entanglement of the orbital angular momentum states of photons. *Nature* **412**, 313-316 (2001).
5. Lavery, M. P. J., Speirits, F. C., Barnett, S. & Padgett, M. J. Detection of a spinning object using light's orbital angular momentum. *Science* **341**, 537-540 (2013).
6. Paterson, L., MacDonald, M. P., Arlt, J., Sibbett, W., Bryant, P. E. & Dholakia, K. Controlled Rotation of Optically Trapped Microscopic Particles. *Science* **292**, 912-914 (2001).
7. Bozinovic, N., Yue, Y., Ren, Y., Tur, M., Kristensen, P., Huang, H., Willner, A. E. & Ramachandran, S. Terabit-scale orbital angular momentum mode division multiplexing in fibers. *Science* **340**, 1545–1548 (2013).
8. Allen, L., Beijersbergen, M. W., Spreeuw, R. J. C. & Woerdman, J. P. Orbital angular momentum of light and the transformation of Laguerre-Gaussian laser modes. *Phys. Rev. A* **45**, 8185–8190 (1992).
9. Uchida, M. & Tonomura, A. Generation of electron beams carrying orbital angular momentum. *Nature* **464**, 737-739 (2010).
10. Khorasaninejad, M., Ambrosio, A., Kanhaiya, P. & Capasso, F. Broadband and chiral binary dielectric meta-holograms. *Science Advance* **2**, 1501258 (2016).
11. Jia, P., Yang, Y., Min, C. J., Fang, H. & Yuan, X. C. Sidelobe-modulated optical vortices for free-space communication. *Opt. Lett.* **38**, 588-590 (2013).
12. Yu, N., Genevet, P., Kats, M. A., Aieta, F., Tetienne, J.-P., Capasso, F. & Gaburro, Z. Light propagation with phase discontinuities: generalized laws of reflection and refraction. *Science* **334**, 333–337 (2011).
13. Lin, D., Fan, P., Hasman, E. & Brongersma, L. M. Dielectric gradient metasurface optical elements. *Science* **345**, 298-302 (2014).
14. Gorodetski, Y., Shitrit, N., Bretner, I., Kleiner, V. & Hasman, E. Observation of optical spin symmetry breaking in nanoapertures. *Nano Lett.* **9**, 3016-3019 (2009).
15. Shaltout, A., Liu, J., Kildishev, A. & Shalaev, V. Photonic spin Hall effect in gap–plasmon metasurfaces for on-chip chiroptical spectroscopy. *Optica* **2**, 860-863 (2015).
16. Miao, P., Zhang, Z., Sun, J., Walasik, W., Longhi, S., Litchinitser, N. M. & Feng, L. Orbital angular momentum microlaser. *Science* **353**, 464-467 (2016).
17. Sun, J., Timurdogan, E., Yaacobi, A., Shah Hosseini, E. & Watts, M. R. Large-scale nanophotonic phased array. *Nature* **493**, 195-199 (2013).
18. Abediasl, H. & Hashemi, H. Monolithic optical phased-array transceiver in a standard SOI CMOS process. *Opt. Exp.* **23**, 6509-6519 (2015).

19. Doylend, J. K., Heck, M. J. R., Bovington, J. T., Peters, J. D., Coldren, L. A. & Bowers, J. E. Two-dimensional free-space beam steering with an optical phased array on silicon-on-insulator. *Opt. Exp.* **19**, 21595-21604 (2011).
20. McManamon, P. An overview of optical phased array technology and status. *Proc. of SPIE* **5947**, 59470I-1 (2005).
21. Mur, J., Kavčič, B. & Poberaj, I. Fast and precise Laguerre–Gaussian beam steering with acousto-optic deflectors. *Applied Optics* **52**, 6506-6511 (2013).
22. Chiu, Y., Burton, R. S., Stancil, D. D. & Schlesinger, T. E. Design and Simulation of Waveguide Electrooptic Beam Deflectors. *Journal of Lightwave Technology* **13**, 2049-2052 (1995).
23. Davis, S. R., Farca, G., Rommel, S. D., Martin, A. W. & Anderson, M. H. Analog, Non-Mechanical Beam-Steerer with 80 Degree Field of Regard. *Proc. of SPIE* **6971**, 69710G-1 (2008).
24. Chan, T. K., Megens, M., Yoo, B. W., Wyras, J., Chang-Hasnain, C. J., Wu, M. C. & Horsley, D. A. Optical beamsteering using an 8×8 MEMS phased array with closed-loop interferometric phase control. *Opt. Exp.* **21**, 2807-2815 (2013).
25. von Neumann, J. & Wigner, E. On some peculiar discrete eigenvalues. *Phys. Z.* **30**, 467 (1929).
26. Plotnik, Y. et al. Experimental observation of optical bound states in the continuum. *Phys. Rev. Lett.* **107**, 183901 (2011).
27. Molina, M. I., Miroshnichenko, A. E. & Kivshar, Y. S. Surface bound states in the continuum. *Phys. Rev. Lett.* **108**, 070401 (2012).
28. Hsu, C. W., Zhen, B., Lee, J., Chua, S.-L., Johnson, S. G., Joannopoulos, J. D. & Soljačić, M. Observation of trapped light within the radiation continuum. *Nature* **499**, 188-191 (2013).
29. Kodigala, A., Lepetit, T., Gu, Q., Bahari, B., Fainman, Y. & Kanté, B. Lasing action from photonic bound states in continuum. *Nature* **541**, 196-199 (2017).
30. Marinica, D. C., Borisov, A. G. & Shabanov, S. V. Bound states in the continuum in photonics. *Phys. Rev. Lett.* **100**, 183902 (2008).
31. Zhen, B., Hsu, C. W., Lu, L., Douglas Stone, A. & Soljačić, M. Topological Nature of Optical Bound States in the Continuum. *Phys. Rev. Lett.* **113**, 257401-5 (2014).
32. Mermin, N. D. The topological theory of defects in ordered media. *Rev. Mod. Phys.* **51**, 591 (1979).
33. Kurosaka, Y., Iwahashi, S., Liang, Y., Sakai, K., Miyai, E., Kunishi, W., Ohnishi, D. & Noda, S. On-chip beam-steering photonic-crystal lasers. *Nature Photonics* **4**, 447-450 (2010).
34. Nakamura, H., Hatano, N., Garmon, S. & Petrosky, T. Quasibound States in the Continuum in a Two Channel Quantum Wire with an Adatom. *Phys. Rev. Lett.* **99**, 210404 (2007).
35. Yang, C., Chen, Y., Wu, S. & Fuh, Y. Independent Manipulation of Topological Charges and Polarization Patterns of Optical Vortices. *Scientific Reports* **6**, 31546 (2016).

Supplementary Material

Integrated and Steerable Vortex Lasers

B. Bahari, F. Vallini, T. Lepetit, R. Tellez-Limon, J. H. Park, A. Kodigala, Y. Fainman, and B. Kanté

Department of Electrical and Computer Engineering, University of California San Diego, La Jolla, CA 92093-0407, USA

bkante@ucsd.edu

1. Fabrication of coherent vortex beam sources

Figure S1 presents a schematic of the seven fabrication steps of a coherent vortex beam source. The active layer is made of InGaAsP multiple quantum wells, epitaxially grown on a lattice-matched InP substrate. The thickness of the InGaAsP is finely controlled to be 300 nm. There is a 10 nm InP protective layer on top of InGaAsP (removed before the fabrication process). To remove the top InP, we dip samples in a chemical solution of HCl:H₂O (3:1) for 60 sec (step 2). A Hydrogen SilsesQuioxane (HSQ) negative tone resist is then coated onto the sample before electron beam lithography (step 3). The written pattern is transferred onto InGaAsP using a dry etch process, namely reactive ion etching, using H₂:CH₄:Ar (40:10:7) for seven minutes. Then we remove the HSQ resist by dipping it into the hydrofluoric acid (step 4). In order to bond the samples onto glass substrates, we use PolyMethyl MethAcrylate (PMMA) A9. After cleaning the glass substrate, we coat PMMA onto glass for 60 sec with a spinning speed and acceleration of 4000 rpm and 1000 rpm/sec, respectively. The sample is then annealed at 185°C for five minutes (step 5). We subsequently bond the InGaAsP on the prepared glass substrate coated with PMMA. Bonding is performed with a clamp to apply uniform pressure. The sample is thus put into an oven for curing at 240°C for one hour under 40 kPa pressure. The curing process last about five hours including about one hour of raising the temperature from room temperature to 240°C, one hour maintained at this temperature and about three hours cooling down the sample to room temperature (step 6). Due to the high pressure and temperature, PMMA infiltrates holes. The last step removes the InP substrate using a chemical solution of HCl:H₂O (3:1). This solution does not etch glass, PMMA, and InGaAsP. The whole etching process to remove the InP lasts about one hour. This step is also visually controllable, because InGaAsP is perfectly crystalline and is thus flat and visually reflective, whereas InP becomes rough during etching. When hydrochloric acid reaches InGaAsP, etching stops. We then remove the sample from the solution and rinse it with Deionized (DI) water (step 7). Figure S2a shows an optical microscope image of the final sample containing different periodic arrays with different radii. The zoom-in image of one of arrays with a size of 200×200 unit cells, is shown in Fig. S2b. Scanning Electron Micrograph (SEM) images of some of the arrays with different radii are shown in Fig. S2c-e

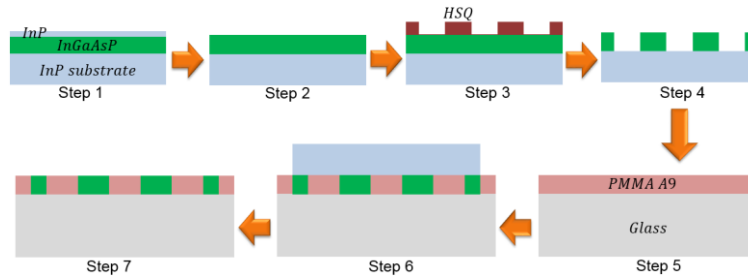


Figure S1 | Schematic of the fabrication steps. **Step 1**: InGaAsP multiple quantum wells wafer. **Step 2**: Removal of the top thin InP layer (thickness = 10 nm). **Step 3**: Coating of Hydrogen SilsesQuioxane (HSQ) resist for e-beam lithography. After the e-beam patterning, the sample is developed. **Step 4**: Dry etching using reactive ion etching to transfer the pattern from HSQ to the InGaAsP. Etching is done by using H₂:CH₄:Ar (40:10:7). **Step 5**: Cleaning of the glass substrate and coating of polymethyl methacrylate on the glass and annealing at 185°C. **Step 6**: Bonding InGaAsP on the glass and curing inside the oven at 240°C for one hour, and pressure of 40 kPa. The whole process takes about five hours including about one hour to raise temperature from room temperature to 240°C, one hour of curing at this temperature, and about three hours to cool down the sample to room temperature. **Step 7**: Removal of InP substrate using a solution of HCl:H₂O (3:1) to selectively etch InP without affecting the rest of materials. The etch time is about one hour.

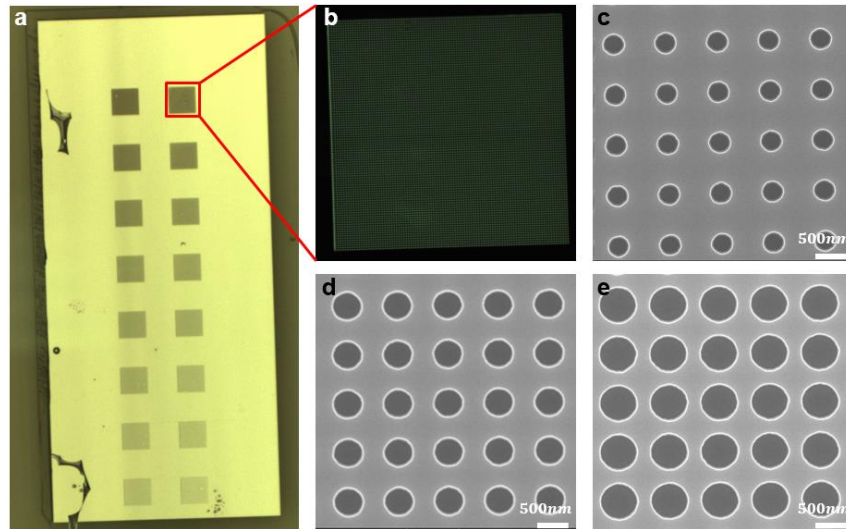


Figure S2 | (a) Microscope image of the fabricated samples. The sample contains different 200×200 arrays with the radii between 180-350 nm. The big pad (shiny surface), with all the arrays is InGaAsP. Some InP residues are visible on the left side of the InGaAsP pad but not on the arrays. (b) Dark field microscope image showing the zoom-in image of one of the arrays. (c-e) Scanning electron micrograph image of the different arrays with different radii, 180 nm (c), 250 nm (d), and 350 nm (e).

2. Characterization of lasers, real/reciprocal spaces and topological charge measurements

Figure S3 shows the schematic of the set-up used to characterize our samples. We use a high-energy laser source with a wavelength of 1064 nm as pump beam to induce population inversion in the InGaAsP. By using an attenuator and a power detector, the power of the pump laser illuminating the sample is finely controlled. Also, the spot width of the pump laser, which initially is 3 mm^2 , is reduced and collimated using two lenses (lenses 1 and 2) before reaching the objective lens. We use an objective lens with a numerical aperture and magnification of 0.4 and X20, to pump the sample and collect the emission simultaneously. The emitted power from the sample, which is in the wavelength range of 1400-1700 nm, is directed to the monochromator (CVI Digikrom DK480) in conjunction with a cooled InGaAs detector in lock-in detection configuration. In the same set-up, by using a removable mirror in the path of the emission beam, we can direct the light to an infrared camera for real space or reciprocal space imaging by putting the camera in the real plane or Fourier plane, respectively. To perform interference measurements, we place the configuration shown in the inset of Fig. S3 in the emission path. The configuration consists in two beam splitters and two mirrors mounted on a translation stage, enabling a fine control of the optical path difference between the two interfering beams.

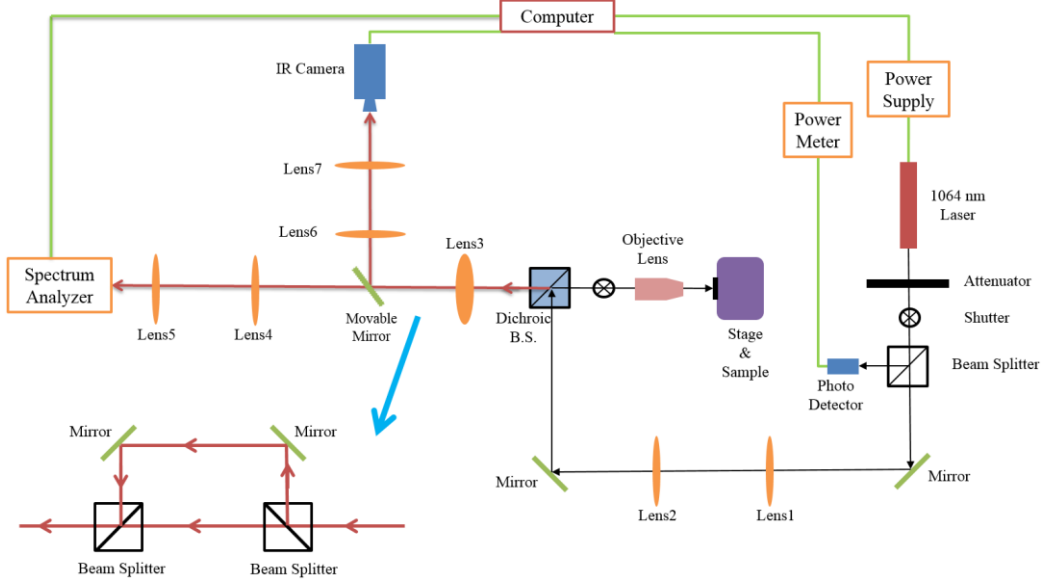


Figure S3 | Schematic of the set-up used for measurements. The incident pump power on the samples is finely controlled using a photodetector, and the emission from the samples is directed to a monochromator for photoluminescence measurements. Real space and reciprocal space imaging are performed by directing the emission toward the camera. The configuration shown in the figure is for real space imaging. The inset shows the interference set-up configuration, which contains two beam splitters and two mirrors mounted on a translation stage to control the optical path.

3. Simulation of devices

We used a finite-element simulation tool (COMSOL Multiphysics) to perform eigen-mode calculations. Simulations are performed on a unit cell with periodic boundary condition, and for every momentum (k_x, k_y) in the 1st Brillouin zone, the complex eigen-frequencies are computed. Figure S4 shows the quality factor map in the 1st Brillouin zone for all three modes shown in Fig. 1c. Mode 1 has a large quality factor at the center of the 1st Brillouin zone (Γ point), while modes 2 and 3 have large quality factors along ΓM and ΓX directions, respectively.

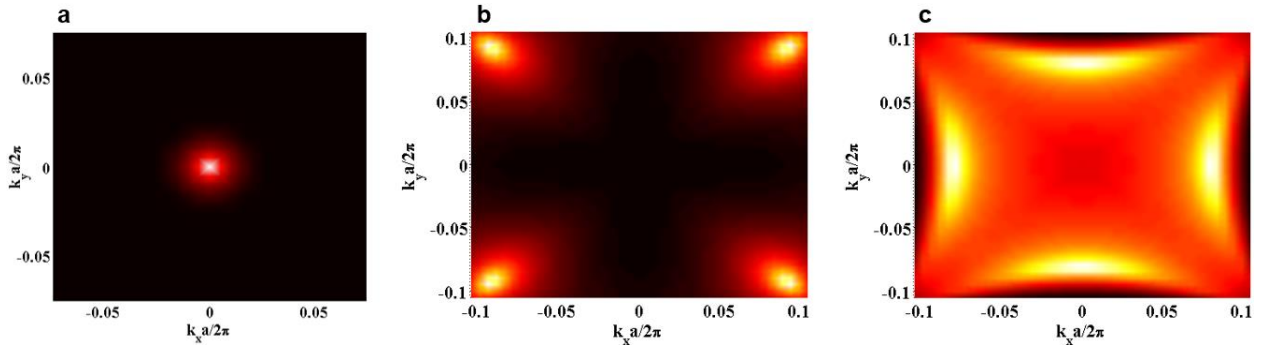


Figure S4 | Quality factor map in the Brillouin zone for modes 1 (a), 2 (b), and 3 (c). For the simulation, we used a unit cell with periodic boundary conditions in the x-y plane, and Perfectly Matched Layers (PML) in the normal direction. The substrate is glass with a refractive index of 1.5, while the cladding is air. PMMA used for bonding the InGaAsP onto glass has a refractive index of 1.5.

Far-field amplitudes and polarizations were extracted from simulations. To calculate the topological charge associated to a singular point, we use the far-field information to calculate the polarization rotation on any arbitrary closed loop, C , which encloses the singular point in the Brillouin zone. The topological charge is calculated using Eq. 1¹⁻³

$$q = \frac{1}{2\pi} \oint_C \nabla_k \phi(\mathbf{k}) \cdot d\mathbf{k}, \quad (1)$$

where $\phi(\mathbf{k}) = \arg[c_x(\mathbf{k}) + ic_y(\mathbf{k})]$, and c_x/c_y are x/y components of the averaged field, $\langle \mathbf{u}_k \rangle$, and \mathbf{u}_k is defined as the periodic part of the Floquet-Bloch modes, $\mathbf{E}(\mathbf{r}, \mathbf{k}) = e^{i\mathbf{k}\cdot\mathbf{r}}\mathbf{u}_k(\mathbf{r})$. Following this procedure, topological charges of -1, -1, and +1 were obtained for modes 1, 2, and 3, respectively.

From near-fields, the far-field was calculated by using near- to far-field transformation⁴. Since we pumped uniformly a large area (more than 50×50), we repeated the unit cell field profile in a large area to emulate the experiment. It is important to note that the Floquet-Bloch phase, $e^{i\mathbf{k}\cdot\mathbf{r}}$, should be accounted for when repeating the unit cell field profile. Above $R = 250$ nm, the laser is operating on mode 1, while below this radius it operates on mode 3. Figure S5 shows the far-field pattern of the laser in which mode 1 is emitting normal to the surface and is doughnut-shaped (Fig. S5a), while mode 3 is emitting at an angle, and is tilted doughnut-shaped (Fig. S5b).

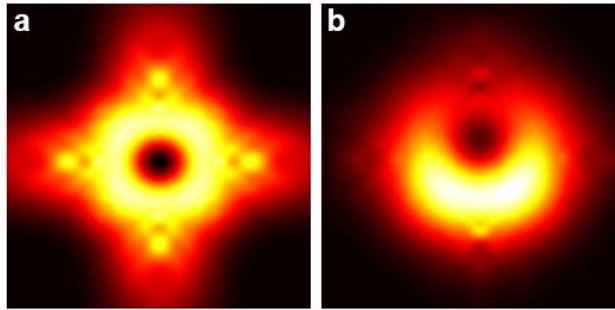


Figure S5 | Far-field patterns of the modes (a) mode 1, and (b) mode 3. To calculate the far-field profile, we extracted the near-field information from each eigen-mode, and repeated it in a large area by taking into account of the Floquet-Bloch phase. Near-field to far-field transformations were then used to calculate the far-field pattern.

4. Controlling the number of beams with boundaries

The fabricated arrays are quite large arrays with dimensions of 200×200 unit cells. The four-fold symmetry, i.e., invariance under 90° rotation implies that any singular state in reciprocal space must have the same symmetry. Consequently, four beams in the emission should be observed (Fig. 2c-f). However, by controlling, for example, the in-plane feedback between the Floquet-Bloch waves in certain directions we can actually control the number of beams. For instance, by choosing crystals with different symmetries/dimensionalities, e.g., 1D crystal, which is invariant under 180° rotation (two-fold symmetry), two beams instead of four beams should be observed. Another possible method, which we used here, is to control the in-plane feedback by bringing certain boundaries closer. We fabricated several arrays with different sizes of unit cells in x and y directions, 10×200 , 15×200 , and 25×200 . The in-plane feedback along the short direction is drastically reduced, almost suppressed, while it remains the same in the long direction.

It is worth noticing that emitted beams do not destructively interfere with each other to cancel the vortex because, the four beams lasing along the four equivalent ΓX directions carry the same topological charges but in four different directions. They are only cancelled when the radius is close to the $R \sim 250$ nm, and mode 2 (lasing along ΓM), which has the opposite topological charge, becomes degenerate with mode 3.

Figure S6 shows SEM images of arrays with different sizes. We performed reciprocal space imaging (Fig. S7), which reveals that for 10×200 , and 15×200 arrays there are only two beams rather than four beams along ΓX . However, arrays of 25×200 are large enough to induce sufficient in-plane feedback along both directions of periodicity to enable lasing.

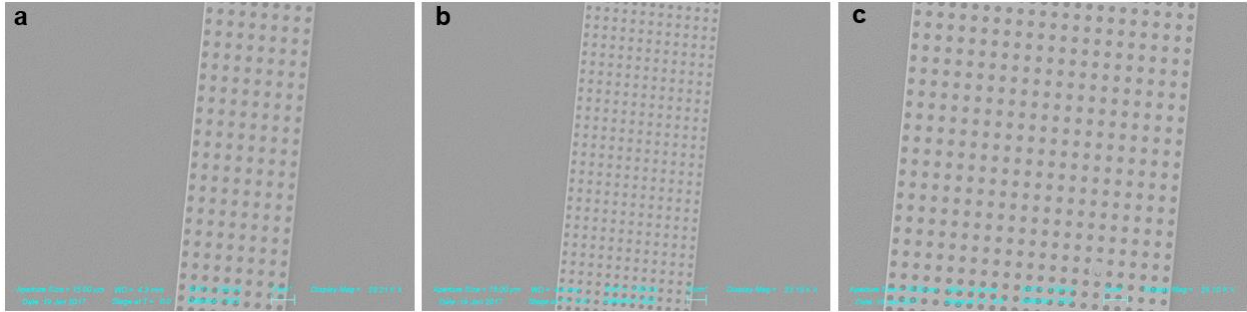


Figure S6 | SEM image of arrays with dimensions of (a) 10×200 , (b) 15×200 , and (c) 25×200 .

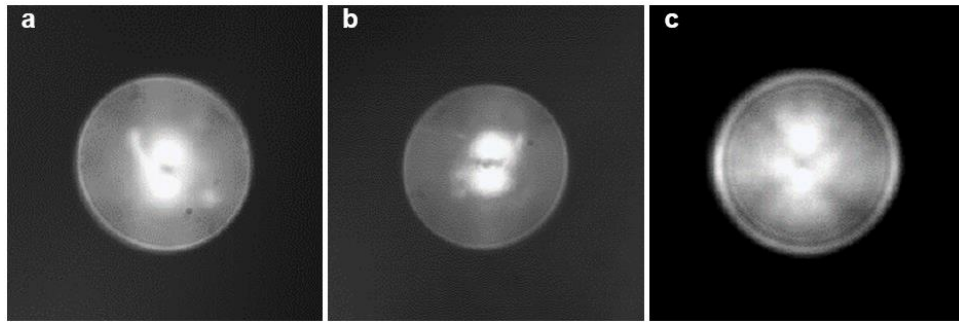


Figure S7 | Reciprocal space measurement for finite arrays with dimensions of (a) 10×200 , (b) 15×200 , and (c) 25×200 . The measurement were done by placing the camera in the Fourier plane. The imaging angle is limited by the numerical aperture (NA) of the objective lens ($NA=0.4$). For the arrays of 10×200 (a) and 15×200 (b) there are two beams along ΓX directions, but for the array of 25×200 (c) there are four beams along four equivalent ΓX directions. The two beams along the vertical axis are brighter than the other two along the horizontal axis. By increasing the size of the array (>25 unit cells), all the four spots tend to become the same.

5. Effective gain and far-field patterns

For larger radii ($R > 250$ nm), mode 1 is the only one with a large quality factor. However, for radii below $R = 250$ nm, modes 2 and 3 also have large quality factors and gain competition then takes place. In the gain spectrum, mode 3 experiences more gain because it has shorter wavelength compared to the other two modes, and mode 1 experiences less gain because it has longer wavelength (Fig. S8a). Additionally, the field intensity confinement inside the gain material for mode 3 is larger than mode 1 and 2 (Fig. S8b), which ultimately results in larger effective gain for mode 3 (Fig. S8c). Therefore, mode 3 lases with a smaller threshold power compared to the other modes. By increasing the pump power, mode 2 also starts lasing as shown in Fig. 4. However, the threshold power of mode 1 is comparable to the damage threshold of the gain material for small radii.

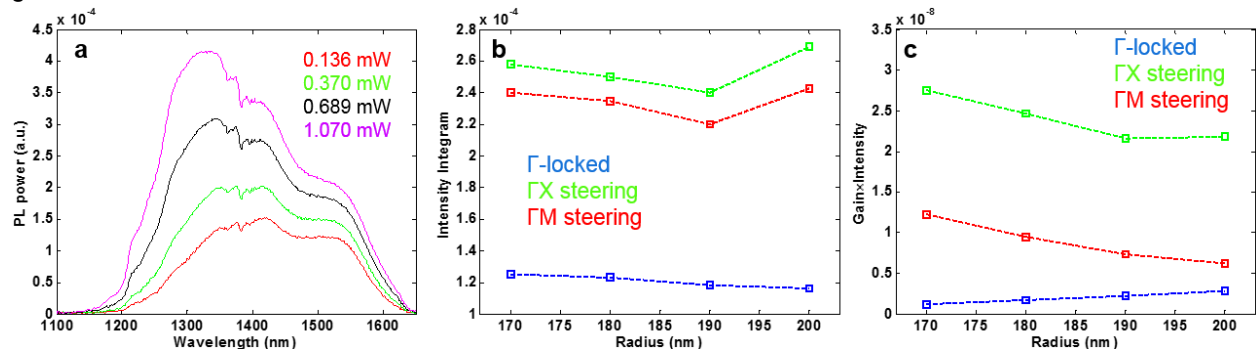


Figure S8 | (a) Gain spectrum measurement of the unpatterned InGaAsP, bonded on a glass substrate using PMMA, as a function of pump power. (b) Calculated integrated intensity of modes 1-3 inside the volume of the gain material (InGaAsP) in a unit cell. (c) Multiplication of the gain and the intensity of the field inside the gain material to evaluate the effective gain for modes 1-3. Mode 3 has larger effective gain than the other modes in a radius range of 170-200 nm, where all three modes have large quality factors.

Figure S9 shows far-field measurements for arrays with different radii. To measure the far-field pattern, we place the movable mirror, shown in Fig. S3, to direct the emission beam toward the camera. The measured far-field patterns agree with simulations shown in Fig. S5. By using a linear polarizer in the path of the emission beam, we observe a two-lobed intensity pattern that rotates by rotating the polarizer. Similar results were obtained for all arrays with different radii further confirming the doughnut-shaped far-field patterns.

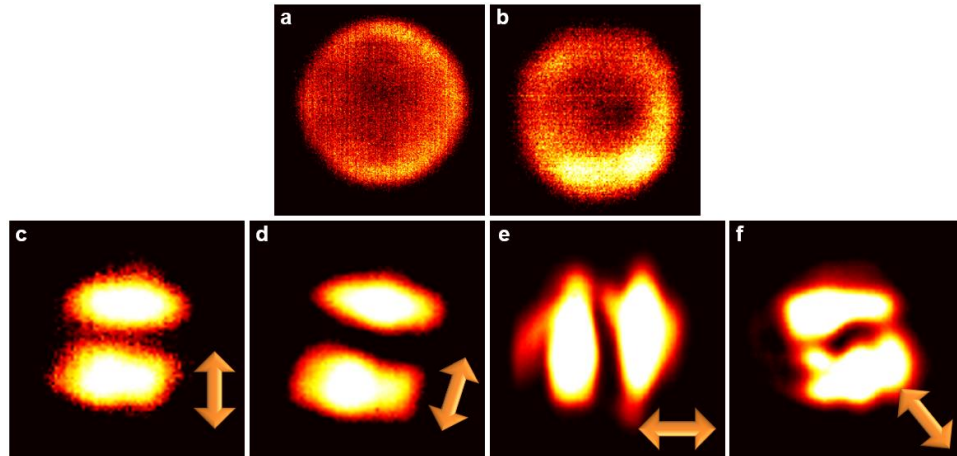


Figure S9 | Far-field measurements of two different arrays with radii of (a) 250 nm, and (b) 225 nm. To measure the far-field patterns, we put the movable mirror in the emission path to direct the beam to the camera. For the array with a radius of 250 nm (shown), the insertion of a linear polarizer in the emission path of the lasers with an angle of (c) 0°, (d) 30°, (e) 90°, and (f) -45° results in the observation of two-lobe shaped patterns coming from doughnut-shaped mode. The arrows in the inset show the direction of the polarizer.

1. Gbur, G. & Tyson, R. K. Vortex beam propagation through atmospheric turbulence and topological charge conservation. *Opt. Soc. Am. A* **25**, 225-230 (2008).
2. Zhen, B., Hsu, C. W., Lu, L., Douglas Stone, A. & Soljačić, M. Topological Nature of Optical Bound States in the Continuum. *Phys. Rev. Lett.* **113**, 257401-5 (2014).
3. Mermin, N. D. The topological theory of defects in ordered media. *Rev. Mod. Phys.* **51**, 591 (1979).
4. C. A. Balanis, *Antenna theory: analysis and design*, (3rd edition, John Wiley & Sons, New Jersey, 2005, Ch. 2 and 5).